Editors' Suggestion

Diffusion characteristics of air pockets on hydrophobic surfaces in channel flow: Three-dimensional measurement of air-water interface

Hyunseok Kim and Hyungmin Park*
Department of Mechanical & Aerospace Engineering, Seoul National University, Seoul 08826, Korea

(Received 15 February 2019; published 3 July 2019)

To effectively apply the superhydrophobic surface for flow control, it is necessary to understand the effect of air-water interface shape on the diffusion characteristics of trapped air pockets. In the present work, using the reflection interference contrast microscopy, we directly measure the temporal variation of the three-dimensional shape of the air-water interface formed on submerged hydrophobic surfaces in a channel flow. The grate and the circular hole are considered a roughness feature, its size is varied between 80 and 200 μm, and the Reynolds numbers of 1850 and 5000 are considered based on channel half-height and bulk velocity. The temporal variation of the height, the curvature of the air-water interface, and the corresponding diffusion length is measured, and the diffusion process is classified into three phases. For each phase, the diffusion characteristics are analyzed in relation to the roughness structure type, size, and Reynolds number. Based on the analysis, we propose a scaling relation for the Sherwood number (dimensionless diffusion length). For the first two phases when the interface is pinned at the roughness edge, the Sherwood number is determined by the interface curvature (i.e., the contact angle between the interface and the roughness sidewall), but it is scaled with the Peclet number (the ratio between the shear rate and the diffusion rate) for the last phase when the interface is depinned and moves downward. These relations are also validated with the data available in the literature, and we think this is useful as a simple guideline to design a roughness geometry for the superhydrophobic surfaces.

DOI: 10.1103/PhysRevFluids.4.074001

I. INTRODUCTION

When the underwater surface is treated to have superhydrophobicity, it is known that an apparent slip is induced between the water flow and the solid surface. This nonwetting superhydrophobic (SHPho) surface has micro- and/or nanosized roughness features on it, and thus the generation of a surface slip has been attributed to the air pockets (so-called plastron) trapped between roughness [1,2]. While the magnitude of a surface slip can be predicted and controlled by the combination of a roughness geometry and flow condition in a well-controlled laboratory environment [3–7], it is also true that more investigations are necessary to test its potential as flow-control methods to achieve various purposes in practical fields [8]. Obviously, the most important application is to reduce the skin-friction drag in wall-bounded shear flows like a channel and boundary layer flow [6,9–13], and a meaningful amount of drag reduction can be achieved on well-designed SHPho surfaces even in a turbulent flow. A slip boundary condition on a fluid-solid interface also results in a separation delay or wake modification in the flow around a bluff or streamlined body [14–16] and a rotating blade [17]. Since the basic idea behind these flow controls is the existence of a free interface

*Author to whom all correspondence should be addressed: Also at Institute of Advanced Machines and Design, Seoul National University, Seoul 08826, Korea; hminpark@snu.ac.kr

between water flow and solid surface, it is necessary to maintain it in a proper shape to ensure the targeted flow control performance [11,12,18,19]. It is therefore critical to note that the surface slip expected on a flat interface is not achieved on a curved air-water interface, and the drag also tends to increase [20–22]. In this regard, Davis and Lauga [23] and Crowdy [24,25] proposed a theoretical prediction on the change in a slip length depending on the shape of an air-water interface. Recently, Ageev *et al.* [18], based on their numerical simulation, explained that the reduction of the effective slip in a curved meniscus is caused by the distorted streamlines near the air-water interface, as other studies have addressed.

Due to this importance of interface dynamics, recent studies have employed various approaches to consider the curved interface shape to assess the stability (i.e., lifetime) of the air pockets, but the unsteady effect of varying interface shape was not fully examined [26–31]. Numerical (or analytical) investigations have in general established the equation of motion (for the interface) based on the balance in the force (pressure) or energy. It is solved under the assumption that the air-water interface is in a quasisteady equilibrium state and the trapped air follows the ideal-gas equation. The initial shape of an air-water interface was assumed to be flat or concave. To describe the temporal variation in the volume of trapped air pockets, Henry's law is adopted to represent air diffusion due to the concentration difference. It was suggested that the plastron longevity is proportional to the roughness height, but inversely proportional to the spacing between roughness asperities [26,27,30]. In addition to the model approach, several studies experimentally measured the temporal behavior of an air-water interface under different flow conditions. The collective lifetime of plastron was indirectly measured by observing the area fraction of survived air pockets optically on a fully immersed SHPho surface [32–34]. Recently, the profile of an air-water interface on an individual plastron was measured directly to further validate the developed diffusion model [28,29,31,35]. In these studies, they used a confocal laser scanning microscopy (CLSM) [28,35] or direct optical imaging [29,31] technique. The CLSM technique guarantees a higher spatial resolution but it has a limited temporal resolution, whereas a direct optical imaging can provide a higher temporal resolution with a lower spatial resolution.

Two variables have been used to quantify the diffusion characteristics of a plastron: the invasion coefficient that indicates the volumetric rate of dissolution according to a partial pressure difference [26,27,30], or the diffusion length representing the thickness of a concentration boundary layer [28,29,31]. While it is possible to reasonably predict the temporal behavior (i.e., the process of sagging and pinch-off) of an air-water interface, it is further required to develop a reliable model for this diffusion parameter. To achieve this, a few studies have quantitatively determined the diffusion length of an air pocket on SHPho surfaces under a flowing condition, and they are closer to practical applications [31,35]. Since the diffusion length (l) is nondimensionalized into the Sherwood number as $\mathrm{Sh}_\delta = \delta/l$ (δ is the characteristic length of a system), Xiang *et al.* [35] proposed a relation of $\mathrm{Sh}_\delta \sim \mathrm{Re}_\delta^{1/3}$ (δ is the channel height) in a laminar channel flow ($2 < \mathrm{Re}_\delta < 17$). On the other hand, Ling *et al.* [31] suggested that the inner scale of a boundary layer is useful in establishing the Reynolds number dependency, and they proposed $\mathrm{Sh}_\theta \sim \mathrm{Re}_\tau^{0.913}$ ($\mathrm{Sh}_\theta = \theta/l$ and $\mathrm{Re}_\tau = \delta u_\tau/\nu$) for transitional and turbulent boundary layers ($500 < \mathrm{Re}_\theta < 2300$). Here, δ and θ are a boundary layer and momentum thickness, respectively, and u_τ is a frictional velocity. We think that these relations provide useful information, but they are valid for lower (laminar) Reynolds numbers or they require inner-scale parameters that are not readily available without a refined near-wall liquid-phase velocity measurement.

Another issue arises from the fact that previous studies assumed the initial and/or transient shape of an air-water interface to be always flat or sagged down [26–30,35]. This is not enough to explain the situation of bulged-up interface and transient behaviors reported by some experimental investigations. This is important because these studies have reported the degradation of surface functionalities (e.g., drag reduction) due to the abnormal (especially the bulged-up profile) interface shape [20,21,36,37]. We tried to figure out under which condition the interface has a convex-up curvature, and we found that it is formed right after water flows over the dried hydrophobic surface. That is, previous studies analyzed the interface behavior with water flow on the surface as an

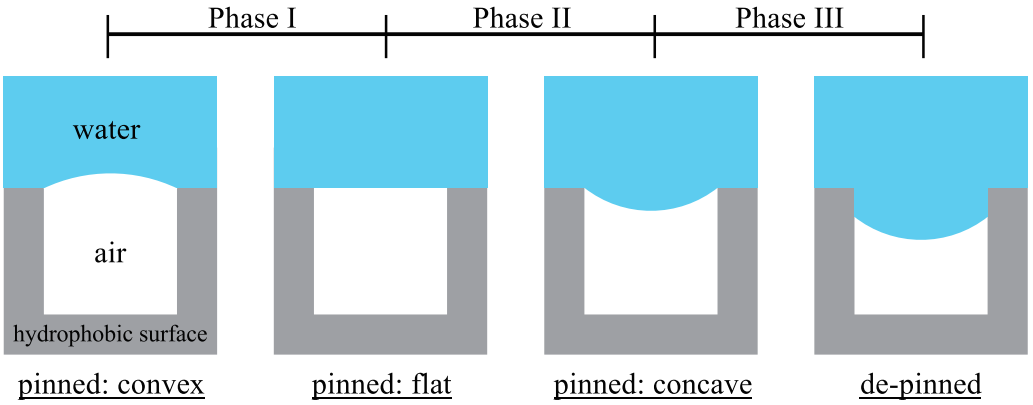

FIG. 1. Schematic diagram for the wetting process occurring on a submerged hydrophobic surface.

initial condition. If we start with a dried condition (air on the surface initially) and water flows over it, the collapsing process of a plastron can be classified into three phases as shown in Fig. 1. Initially, the air-water interface has a convex shape and becomes flat as the diffusion of the air pocket occurs (phase I). With further diffusion, the interface profile becomes sagged down (concave profile) while it is attached to the roughness edge (phase II). When the angle between the interface and the sidewall of the roughness exceeds the advancing contact angle of the SHPho surface, the interface detaches from the asperity of a roughness feature and moves down while maintaining a constant sagging profile (phase III). To the best of our knowledge, this study first identified (visually) the transitions between three possible interface shapes with time and theoretically derived the diffusion characteristics accordingly. On the other hand, it can be said that previous studies considered phases II and/or III during the wetting transition, and the diffusion length was determined solely based on the analysis of phase III [28,29,31,35]. It is clear that the diffusion characteristics, as well as the performance of the SHPho surface, would change a lot during the wetting process, and we need to develop a more accurate diffusion model depending on the phase in a wetting transition.

Therefore, we investigate the diffusion characteristics of air pockets trapped on a hydrophobic surface depending on the phases in a wetting transition. To achieve this, we experimentally measure the three-dimensional behavior of the air-water interface on hydrophobic surfaces in turbulent channel flows using a reflection interference contrast microscopy (RICM) technique [38–41]. For the roughness geometry on the surfaces, we consider grates and circular holes, and the Reynolds numbers of a channel flow are 1850 and 5000 based on the bulk velocity and half channel height. We also derive the equation of a diffusion length depending on the phases in a wetting transition, and we use the measured interface shape to calculate it. Finally, we suggest a diffusion model to estimate the diffusion rate of a plastron in terms of flow variables (outer scale) and geometric parameters. We believe this will enhance our understanding of the hydrodynamics of flow over nonwetting hydrophobic/superhydrophobic surfaces, and provide a simple guideline to devise surfaces with a longer lifetime of trapped air pockets.

II. EXPERIMENTAL SETUP AND PROCEDURES

A. Flow facility and hydrophobic surfaces

Figure 2 shows the experimental setup including the rectangular channel flow with the tested hydrophobic surface that is flush mounted on the channel bottom. The sagging profile of the air-water interface is measured using an inverted microscope (details are explained in Sec. II B). The size of the test section is 1200 mm × 150 mm × 6 mm in the streamwise (x), spanwise (y), and vertical (z) directions. The aspect ratio of the cross section is 25.0, which is sufficiently large to

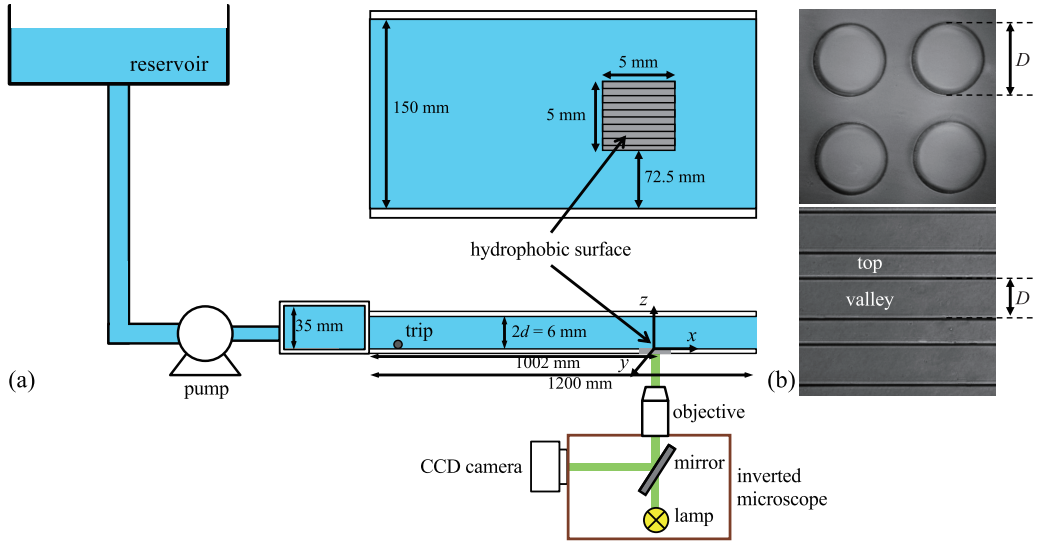

FIG. 2. Experimental setup for the rectangular channel flow with a hydrophobic surface flush-mounted on the bottom wall: (a) front and top views; (b) roughness features of the present test surfaces: hole (top) and grate (bottom).

assume that the flow is two-dimensional [42,43]. As a working fluid, we use deionized (DI) water that is produced via a water purification system and is exposed to the ambient environment for more than two days to be fully saturated with air [28]. We have measured the degree of oxygen saturation in DI water while keeping the same condition of interface measurements using an optical dissolved oxygen meter (ProODO, YSI) that has a measurement resolution of 0.125%. The measurement of oxygen concentration was repeated five times (with five readings per each) for the DI water both stored in the tank and that flows out of the channel exit. It is measured that the oxygen concentration level is maintained as $100.3 \pm 3.2\,\%$ for all cases, confirming that the oxygen level only varies within the range of standard deviation (i.e., maintained to be saturated with air). During the flow test, the timescale of the air diffusion ($t_a = d^2/D_G \simeq 4 \times 10^3$ s, where D_G is the diffusion coefficient of air) is much longer than the timescale of channel flow ($t_f = L/U \simeq 2$ s, where L is the channel length and U is the bulk velocity), thus the oxygen level would not change during the flow test. From the reservoir, DI water is pumped to the channel while its flow rate is controlled. The hydrophobic surface is flush-mounted on the bottom surface of the test section, 1000 mm from the inlet, which is sufficiently far to consider that the flow over the slip surface is fully developed. The considered Reynolds numbers of the water flow are $\mathrm{Re} = 1850$ and 5000, based on the bulk velocity (U, determined from the volume flow rate) and half channel height (d). To ensure a fully turbulent flow over the hydrophobic surface, a trip-wire (whose diameter is about 1.0 mm) is located 5 mm from the inlet to encourage the early transition to turbulence [Fig. 2(a)]. On the other hand, to guarantee the statistically converged data, we have performed 9–19 individual measurements of the interface for each case (while keeping the flow condition the same), and the range of measured data is shown as vertical bars in the figures in Sec. IV.

The considered hydrophobic surfaces (5 mm × 5 mm in size) are fabricated via a soft-lithography on PDMS, which is chosen because it is transparent and thus suitable for the optical measurement of the air-water interface from the bottom. We did not apply additional treatment to the PDMS surface to enhance its hydrophobicity (i.e., longevity of the plastron), because we intended to focus on the wetting transition. For the roughness features, we consider rectangular grates and circular holes [Fig. 2(b)]. A single surface specimen includes 50 grates or 500 holes on it (the gas fraction, defined

TABLE I. Static contact angles (θ_e) and static condition diffusion length ($l_\circ$) measured for the considered hydrophobic surfaces.

Roughness feature	D (μm)	θ_e	$l_\circ$ (μm)
Grate	80	112.9°	5.4
	100	127.4°	5.0
	120	130.1°	4.3
Hole	120	101.4°	4.4
	200	123.1°	6.1

as the planform area fraction of the air-pocket, is 0.5 for the grate and 0.44–0.55 for hole geometry). For the rectangular grate (length of 5 mm), its width (D) is varied as 80, 100, and 120 μm, and the diameter of the hole (D) is set to be 120 and 200 μm. For the grate, we also change its orientation, i.e., longitudinal and transverse ones that are parallel and normal to the flow direction, respectively. It is noted that the feature size of the present surfaces is intentionally designed to be relatively larger than that [$\boldsymbol{O}$(0.1–10) μm] of previous studies because the conditions that are more susceptible to the wetting transition are preferred for our purposes. The depths (H) of grates and holes are all the same as 20 μm. The static contact angle (θ_e) of a water droplet on the present surfaces is measured using a method based on B-spline snakes (active contours) [44] and is summarized in Table I. The static contact angles of the present samples agree well with a previous study [45]. Based on the static contact angles, strictly speaking, the present surface may not be classified as a SHPho surface. However, the models that we have developed to represent the diffusion characteristics are determined by whether the air-water interface is in phases I-II or III, not by the specific value of the apparent contact angle (see Secs. III and IV). Therefore, we think that the results from the present study can be readily extended to the diffusion analysis of gas trapped on SHPho surfaces.

B. Reflection interference contrast microscopy

We use a reflection interference contrast microscopy (RICM) to measure the temporal variation of the air-water interface shape. Basically, RICM is a kind of interferometry, which uses an antiflex technique [46] to improve the signal-to-noise ratio. Thus, it is known to have higher accuracy than other interferometry techniques. Unlike the confocal laser scanning microscopy, the RICM method captures the image of the whole region of interest simultaneously, thus it is appropriate to study the three-dimensional dynamics with more precise measurement.

The present configuration of RICM is shown in Fig. 3(a). The light from the lamp passes through the bandpass filter and turns into a monochromatic light that is guided to the bottom of the surface. This incident light is reflected through two different paths: from the bottom (air-solid interface) and top (air-water interface) of the plastron, respectively [Fig. 3(a)]. The reflected light is digitally recorded by a camera, which shows the interference (fringe) pattern [Fig. 3(b)] according to the optical path difference of received light, i.e., the thickness of the plastron. In the present study, we use an inverted microscope (GX51, Olympus) as a basic frame and a mercury lamp (U-LH100HG, Olympus) as a light source. A bandpass filter with a wavelength of 550 nm and a bandwidth of 50 nm is used to filter the light source into a monochromatic light. Images are taken at a speed of 5 fps using a CCD camera (VH-4mc, Vieworks) with an objective (UPlanFl 10X, Olympus) equipped. The antiflex technique consists of a polarizer, analyzer, and $\lambda/4$-plate, which blocks the noise caused by stray light and improves the signal-to-noise ratio [46].

Assuming that the incident and reflected light is normal to the interface, we can quantify the fringe pattern as an image intensity, $I(x, y)$, with a relation shown below [47],

$$I(x, y) = A(x, y) + B(x, y) \cos\left[\frac{4\pi n_1 h(x, y)}{\lambda}\right] + N(x, y). \tag{1}$$

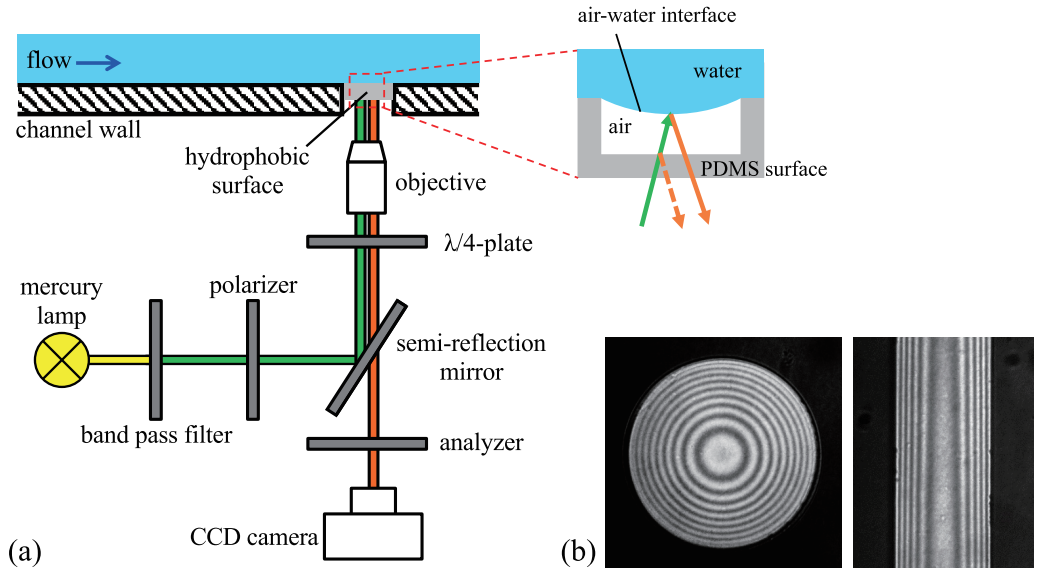

FIG. 3. (a) Setup for the present reflection interference contrast microscopy. (b) Examples of measured fringe pattern for hole ($D = 200$ μm at Re $= 1850$) and grate ($D = 120$ μm at Re $= 1850$).

Here, $A(x, y)$, $B(x, y)$, and $N(x, y)$ represent the background intensity, fringe amplitude, and noise, respectively. On the other hand, n_1 is the refractive index (of air for the present measurement) and λ is the wavelength of incident light (550 nm for this setup). To measure the air-water interface height [$h(x, y)$, plastron thickness], we need a series of preprocessing of the acquired images. First, the noise is removed by applying a 2D Wiener filter to the image, and MO-BEMD [48] is applied to remove the background and highlight the fringe pattern. Finally, the image intensity is normalized by a Spiral-Hilbert transform [49,50]. After we perform the preprocessing, the image intensity can be obtained from Eq. (1) as

$$I_n(x, y) = \cos\left[\frac{4\pi n_1 h(x, y)}{\lambda}\right]. \tag{2}$$

Thus, the local height of the air-water interface $h(x, y)$ obtained by the following equation is used to reconstruct the three-dimensional shape of the interface:

$$h(x, y) = \frac{\lambda\{\cos^{-1}[I_n(x, y)] + 2\pi n\}}{4\pi n_1}. \tag{3}$$

In Eq. (3), order n is determined based on the choice of a reference point. For a spatial reconstruction of interface shape, the center of the fringe patterns is set to $n = 0$, and the instant when the interface is detached from the asperity of roughness feature (the boundary between phases II and III) is set to $n = 0$ for a temporal reconstruction.

To validate the present RICM setup and processing algorithm, we measure the outer profile of a convex lens (Edmund Optics, LENS PCX 25.4 mm DIA $\times$ 76.2 mm FL UNCOATED). Figure 4(a) shows the measured fringe pattern, and we compare the measured profile with the actual value in Fig. 4(b). As shown, the present measurement shows a good agreement with the real profile. The maximum error is 0.03 μm, which is about 6% of the maximum height. The measured curvature deviates from the real one by about 0.8%. The resolution of measurable curvature from the present RICM setup is analytically estimated (i.e., in an ideal condition) as small as $\boldsymbol{O}(10^{-4})$ (please see the Supplemental Material [51] for the details). On the other hand, we checked whether heating by the light source affects the measurement in the present setup. This was tested for the static condition

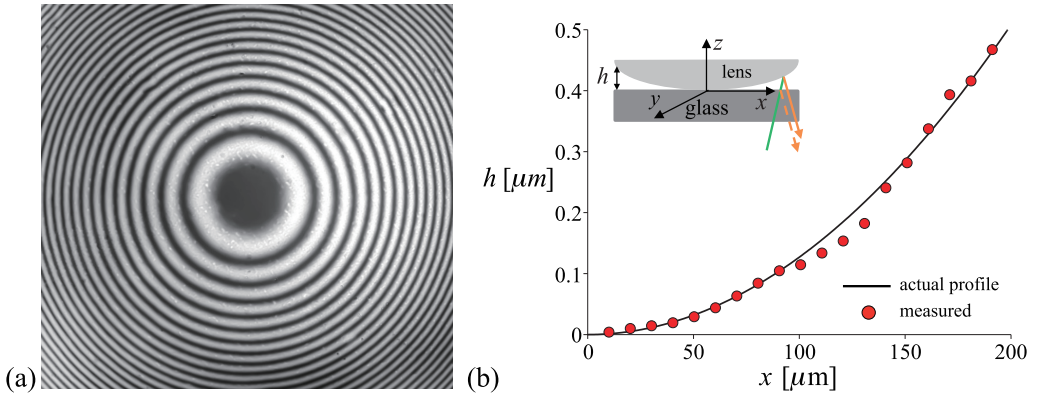

FIG. 4. Validation of the present RICM measurement algorithm and setup: (a) measured fringe pattern of a convex lens; (b) comparison between the actual and reconstructed profiles of the lens, at the center plane ($y = 0$).

(without flow), and the measured diffusion length did not differ much. We think that the time taken for individual measurement is not long enough for the heating effect to show up (please see the Supplemental Material [51] for the details).

III. ANALYTICAL MODEL FOR THE DIFFUSION LENGTH

After we measure the three-dimensional shape of the air-water interface with time, it is necessary to calculate the diffusion length based on it. In this section, we explain how the diffusion length and the measured interface shape are related, depending on three phases about the plastron state as shown in Fig. 1. We start with a single air pocket trapped in a grate or hole on a fully submerged hydrophobic surface (Fig. 5). Due to its geometrical simplicity, here we explain the formulation for the case of the grate (for the hole, the basic idea is exactly the same; see the Supplemental Material [51] for details). To describe the interface geometry, we define h^* as the height of the contact point between the interface and the solid structure, h' as the depth (height) of the sagged (or

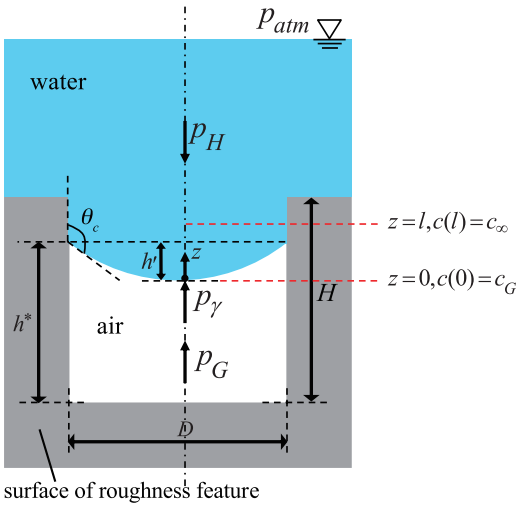

FIG. 5. Schematics of the air-water interface on a grate (not drawn to scale).

bulged-up) portion of the interface, and the contact angle of the interface as θ_c. On the interface, it is considered that the hydrostatic pressure (p_H), capillary pressure (p_γ), air partial pressure in the plastron (p_G), and atmospheric pressure (p_{atm}) are applied and balanced.

To express the transport of air from the plastron, we start with Fick's law, stating that the mass flux of air from plastron to liquid per unit area (J) is proportional to the air concentration (c) gradient, and the proportional constant is a diffusion coefficient of air (D_G),

$$J = -D_G \frac{dc}{dz}. \tag{4}$$

Here, z is the vertical coordinate from the center of the air-water interface (Fig. 5). Assuming that the air diffusion occurs mostly in a thin film (thickness of l) in which there is no mass source or sink, it is derived that $dJ/dz = -D_G(d^2c/dz^2) = 0$. In general, this thin-film approximation has been applied to the mass diffusion problem because of its simple but accurate result. In this case, the film thickness is called a diffusion length of the system [52]. Then, we define the boundary conditions for air concentration as $c(0) = c_G$ and $c(l) = c_\infty$, and the mass flux can be simply expressed as $J \simeq D_G(c_G - c_\infty)/l$. According to Henry's law, the gas pressure inside the plastron is expressed as $p_G = K_H c_G$, where K_H is Henry's constant). Then, Eq. (4) is written as

$$J = \frac{D_G}{lK_H}(p_G - p_\infty). \tag{5}$$

This indicates that the mass flux [$J = (dn_G/dt)/A$, where n_G is the number of air moles in plastron] of gas (air) from the plastron to the surrounding liquid (water) per unit area is proportional to the partial pressure difference of air contained in the plastron and the bulk above (p_∞), but is inversely proportional to the diffusion length (l). Assuming that the trapped air follows the ideal-gas law ($p_G V_G = n_G RT$, where R is the ideal-gas constant) and the water is saturated with air, we can write Eq. (5) as

$$\frac{d}{dt}(p_G V_G) = -\frac{AD_G RT}{lK_H}(p_G - p_\infty). \tag{6}$$

Here, V_G is the volume of the plastron and A is the area of the air-water interface. For a grate, they are calculated as $V_G = Dh^* + D^2[\sin^{-1}(\cos\theta_c) - \cos\theta_c \sin\theta_c]/(4\cos^2\theta_c)$ and $A = D\sin^{-1}(\cos\theta_c)/\cos\theta_c$, respectively.

As we have explained above, we have exposed the water to the atmosphere for more than two days, and the bulk water is fully saturated with air. The pressure components acting on the interface are considered to be balanced in a quasistatic equilibrium state, such as $p_G = p_H + p_{\text{atm}} + p_\gamma$. In the case of a grate, the capillary pressure at the interface is given as $p_\gamma = 2\gamma\cos\theta_c/D$ (γ is the surface tension). Since the local height of the interface is expressed as $h = h^* + h'$, the following relation is derived from Eq. (6):

$$\Pi_0 \frac{dh^*}{dt} + \Pi_1 \frac{dh'}{dt} = -\frac{A}{D}\frac{D_G RT}{K_H l}\left(p_H + \frac{2\gamma\cos\theta_c}{D}\right). \tag{7}$$

Here, Π_0 and Π_1 include the pressure in the plastron (p_G) and the information on the air-water interface geometry, and they are written as Eqs. (8) and (9), respectively,

$$\Pi_0 = p_H + p_{\text{atm}} + \frac{2\gamma\cos\theta_c}{D}, \tag{8}$$

$$\Pi_1 = (1+\sin\theta_c)\left[\frac{4\gamma h^*\sin\theta_c}{D} + \gamma\left(\frac{\cos\theta_c - \sin\theta_c\sin^{-1}(\cos\theta_c)}{\cos^2\theta_c} + \cos\theta_c\right)\right.$$
$$\left. - \frac{D(p_H + p_{\text{atm}})[\sin\theta_c\sin^{-1}(\cos\theta_c) - \cos\theta_c]}{\cos^3\theta_c}\right]. \tag{9}$$

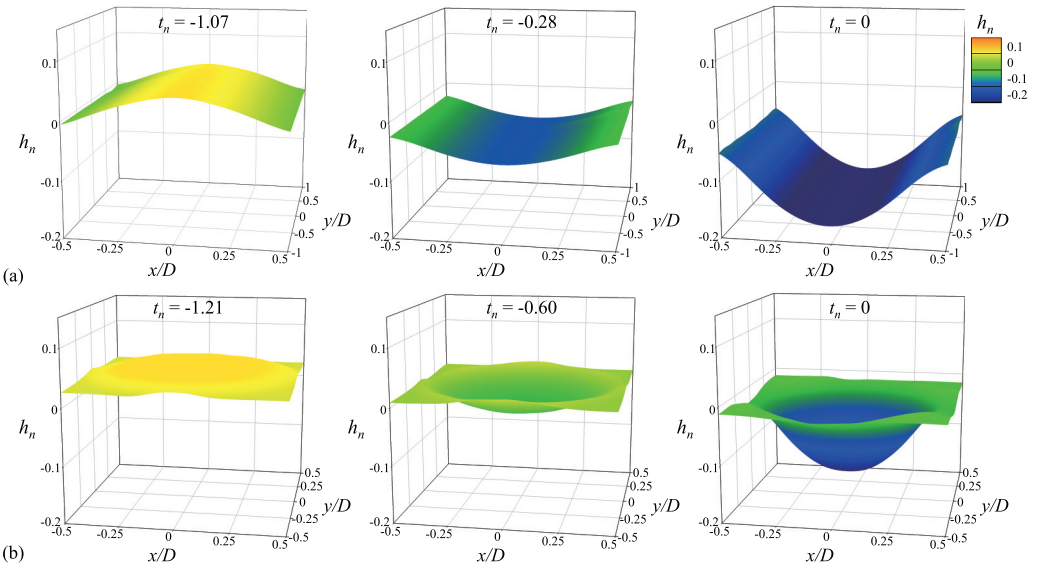

FIG. 6. Three-dimensional air-water interface shape for (a) transverse grate ($D = 120\ \mu$m) and (b) hole ($D = 200\ \mu$m) at Re = 1850: phase I (left), phase II (middle), and phase III (right). Here, $t_n = 0$ is the instant when phase III starts (interface depinning) and x is the streamwise direction.

We can rearrange Eq. (7) for the diffusion length (l) as in Eq. (10),

$$l = \frac{-\frac{A}{D}\frac{D_G RT}{K_H}\left(p_H + \frac{2\gamma\cos\theta_c}{D}\right)}{\Pi_0 \frac{dh^*}{dt} + \Pi_1 \frac{dh'}{dt}}. \tag{10}$$

For phases I and II, the air-water interface is pinned at the roughness edge ($dh^*/dt = 0$) and the sagged profile is maintained after the depinning at phase III ($dh'/dt = 0$). Therefore, the diffusion lengths for phases I and II ($l_{\mathrm{I-II}}$) and III (l_{III}) are further expressed as Eqs. (11) and (12), respectively.

$$l_{\mathrm{I-II}} = \frac{-\frac{A}{D}\frac{D_G RT}{K_H}\left(p_H + \frac{2\gamma\cos\theta_c}{D}\right)}{\Pi_1 \frac{dh'}{dt}}. \tag{11}$$

$$l_{\mathrm{III}} = \frac{-\frac{A}{D}\frac{D_G RT}{K_H}\left(p_H + \frac{2\gamma\cos\theta_c}{D}\right)}{\Pi_0 \frac{dh^*}{dt}}. \tag{12}$$

From these models, it is understood that the temporal change of the diffusion length depending on the state of plastron can be determined by measuring the air-water interface height (h^* and h') over time. Again, a similar relation can be derived for the hole geometry, and the detailed formulation is given in the Supplemental Material [51].

IV. RESULTS AND DISCUSSIONS

A. Temporal variation of air-water interface

As we have introduced, with the present RICM method it is possible to measure the three-dimensional interface shape with a temporal resolution that is sufficient to analyze the variation of interface curvature over time. Figure 6 shows examples of the three-dimensional air-water interface shape at each phase reconstructed from the fringe pattern measured with the RICM technique. Shown in the figure are the cases of the transverse grate ($D = 120\ \mu$m) and hole ($D = 200\ \mu$m) at Re = 1850. For each case, three representative instants corresponding to the phases classified in

TABLE II. Duration of the phase II (t_{II}), measured from the instant when the curvature (κ_n) has the minimum value to the instant when κ_n starts to saturate.

Roughness feature	D (μm)	t_{II} (s)
Longitudinal grate	80	49.52
(Re = 1850)	100	58.69
	120	80.33
Transverse grate	80	50.99
(Re = 1850)	100	51.85
	120	92.43
Hole	120	54.87
(Re = 1850)	200	72.09
Hole	120	32.67
(Re = 5000)	200	56.40

Fig. 1 are shown. Here, the local interface height is normalized as $h_n = h/H$ and the dimensionless time $t_n = (t - t_\circ)/t_{II}$ is used, where t_{II} is the duration of phase II (summarized in Table II) and $t = t_\circ$ is the instant of interface depinning. It is clearly shown that the air-water interface is transitioned from a convex to a concave shape, as the diffusion of trapped air progresses. On the other hand, the interface shape is spherical and cylindrical for the hole and grate, respectively, i.e., the cross-sectional shape is part of a circle, which is determined by the Young-Laplace equation. Thus, it is symmetric with respect to the center plane of roughness feature, and we will use the interface height (h_c) at the center and curvature (κ) as representative parameters to characterize the diffusion characteristics.

As an example to show how to quantify the measured interface shape, the temporal variation of normalized interface center height ($h_{cn} = h_c/H$) and the curvature for the cases shown in Fig. 6 are plotted in Fig. 7. The curvature of the interface ($\kappa = 1/R$) is nondimensionalized as $\kappa_n = (D/2)/R = |\cos\theta_c|$ (where the radius of curvature, R, is obtained by fitting the reconstructed air-water interface with a circle and sphere for the grate and hole, respectively). It is noted that, by definition of dimensionless time t_n, the phase transition occurs at $t_n = -1.0$ and 0 between phases I-II and II-III, respectively. In Fig. 7, it is shown that the interface height decreases gradually with time, but its sagging velocity (slope of variation) increases with the wetting transition. On the other hand, the interface curvature varies distinctively according to the phases. In phase I, the curvature decreases to the minimum value, since the interface shape changes from convex to flat as the diffusion progresses. Ideally, the curvature should reach zero at the boundary between the

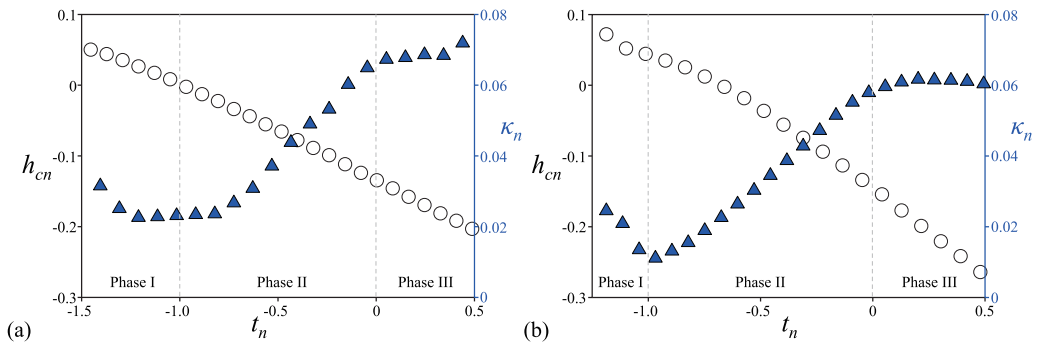

FIG. 7. Temporal variation of normalized interface center height (h_{cn}, ○) and normalized curvature (κ_n, ▲) for (a) the transverse grate ($D = 120$ μm) and (b) the hole ($D = 200$ μm) at Re = 1850.

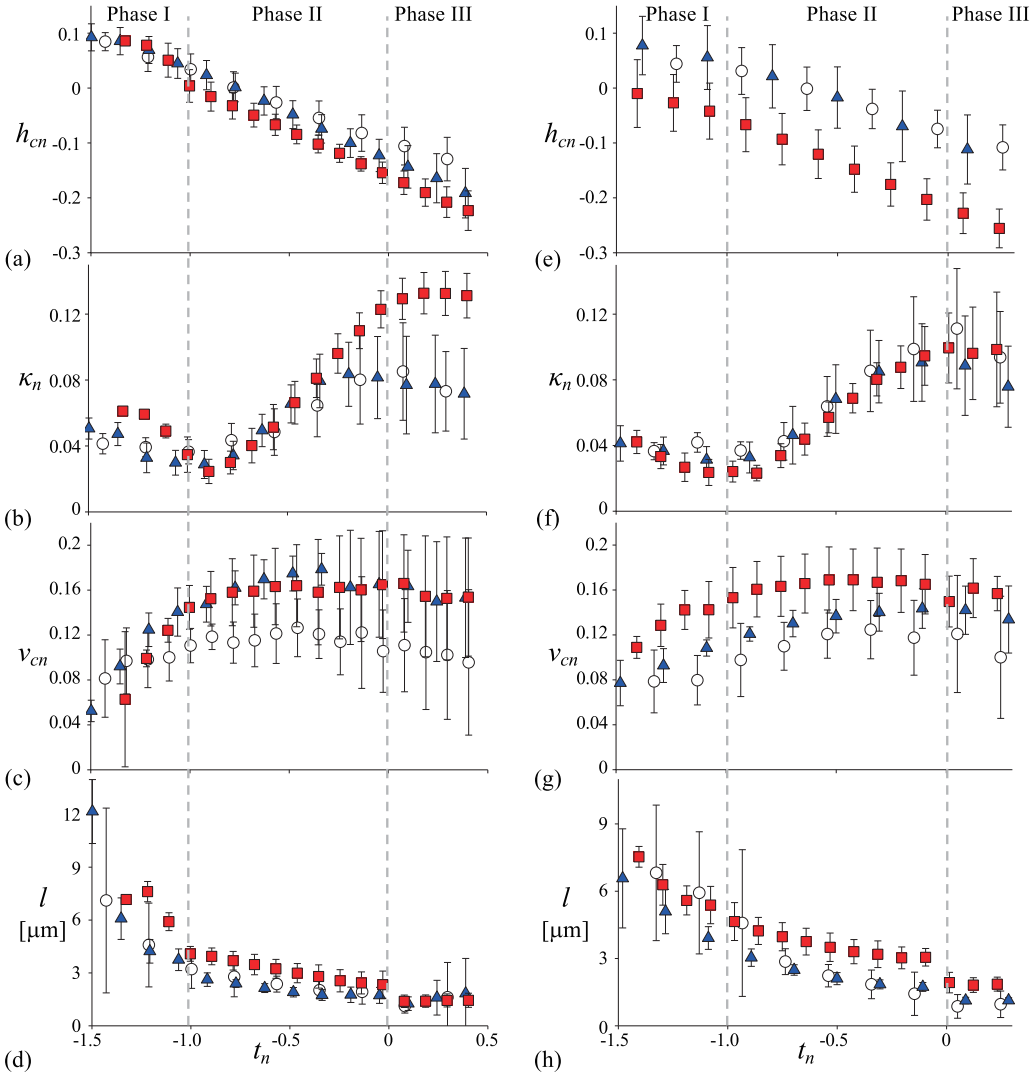

FIG. 8. Diffusion characteristics of a grate geometry aligned to the (a)–(d) longitudinal and (e)–(h) transverse directions at Re = 1850: (a), (e) normalized interface center height (h_{cn}); (b), (f) normalized curvature (κ_n); (c), (g) normalized sagging speed (v_{cn}); and (d), (h) diffusion length l for phases I-II [Eq. (11)] and III [Eq. (12)]. ○, $D = 80$ μm; ▲, 100 μm; ■, 120 μm.

phases I and II, but the accurate measurement of the flat interface is not possible because a flat interface has no fringe pattern by which we measure the three-dimensional interface shape. Thus, the minimum value of κ_n in the figure corresponds to the instant when the fringe pattern starts to show up and it is possible to calculate the height and curvature from it, not relevant to the resolution of our measurement (see Sec. II B). With a further diffusion of air, the interface enters phase II and the curvature increases again as the interface sags down with the interface attached to the roughness edge. After the depinning of the interface (phase III), it tends to maintain its shape while moving downward, so the curvature saturates to a constant value.

Figure 8 shows the temporal variations of the interface center height (h_{cn}), interface curvature (κ_n), sagging speed of interface center ($v_{cn} = |dh_{cn}/dt_n|$), and the estimated diffusion length (l)

corresponding to each phase, for longitudinal (LG) and transverse (TG) grates, measured at Re = 1850. Since the interface we have measured is initially convex, its height at the center (h_{cn}) starts with a positive value and decreases gradually with time [Figs. 8(a) and 8(e)]. For both longitudinal [Fig. 8(a)] and transverse [Fig. 8(e)] grates, the interface height tends to increase with decreasing width (D) of the grate across all the phases that we have classified. For all cases, the interface curvature follows the trends shown in Fig. 7; that is, it initially decreases to the minimum value at phase I and increases back while entering phase II. As the interface detaches off the roughness edge (phase III), the interface curvature is maintained to be almost the same. While the initial curvature on the longitudinal grate is slightly larger as the grate width increases, it shows little difference depending on the grate width for the case of the transverse grate [Figs. 8(b) and 8(f)]. This is because for the transverse grate, the influence of shear by the water flow is mostly to push the interface downward, not shearing along the streamwise direction. For both alignments, the interface sagging speed increases steeply in phase I, which becomes mild and saturated in phases II and III, respectively [Figs. 8(c) and 8(g)]. The sagging speed tends to increase as the grate width increases, but more data are needed to establish a more accurate relation between them.

This understanding can be further supported by examining the variation of diffusion length that we have formulated above. As it stands for, i.e., the thickness of the concentration boundary layer, the diffusion takes place faster as the diffusion length is smaller. As shown in Figs. 8(d) and 8(h), the diffusion length decreases rapidly in phase I and then quite slowly in phase II, which agrees with the trend of sagging (i.e., diffusion) speed across the phases [Figs. 8(c) and 8(g)]. Previously, it was shown that the slip length on a convex interface decreases as the interface curvature increases [23,24]. Since the concentration boundary layer thickness where the diffusion occurs is closely related to the velocity boundary layer thickness [52,53], the relation between them has been examined. As introduced earlier, Ling *et al.* [31] suggested the relation of $\mathrm{Sh}_\theta \sim \mathrm{Re}_\tau^{0.913}$ for SHPho surfaces (transverse grate) under a turbulent boundary layer flow ($\mathrm{Re}_\tau = 200$–1000). Here, Sh_θ and Re_τ are the Sherwood number based on momentum thickness and the frictional Reynolds number of the reference flow, respectively. This shows that the plastron diffusion rate increases with the enhanced shear stress. Thus, it is understood that the shear-induced diffusion of trapped air would be accelerated as κ_n increases (i.e., slip length decreases) in phases II and III. In general, the diffusion length is proportional to the contact area between a solvent and a solute [52], thus it is reasonable to think that the diffusion length will increase as the grate width (area of the air-water interface) increases. This is roughly observed in phases I and II (the case of $D = 120$ μm shows the largest l) for both longitudinal and transverse grates. Also, this explains why the time taken for phase II (t_{II}) is extended as the grate width increases, as shown in Table II. In phase III, although the values of diffusion length are quite small, this trend is still maintained and the case of $D = 120$ μm shows the largest l. While the interface sagging is the fastest in the interface center during phase I-II, the entire interface sags downward with the same speed in phase III. Therefore, the mass flux of air diffusing outward becomes larger in phase III and this change results in the slight decrease in diffusion length after detachment. This explanation needs to be supported by more rigorous investigations, e.g., about the dynamics of moving three phase contact line. On the other hand, it has been reported that the effective slip length with the transverse grate is much smaller than that with the longitudinal one [3], and furthermore the nonlinear process of turbulence generation by no-slip/shear-free alternating boundary conditions via transverse grates has been suggested as a reason for skin-friction drag increase for some cases [10,54]. This change in the flow characteristics over the superhydrophobic surface may affect the diffusion characteristics of trapped air pockets; e.g., faster diffusion for the case of a transverse grate. It is interesting to see that the grate orientation does not affect the diffusion length significantly. For the present cases, it is notable that the decreasing slope of diffusion length in phase I is much steeper for the case of a longitudinal grate, but the difference due to the grate orientation is negligible in phases II and III. It is possible that the streamwise length of the superhydrophobic surface should be sufficiently long to evaluate the effect of grate orientation further, which will be meaningful as a future study.

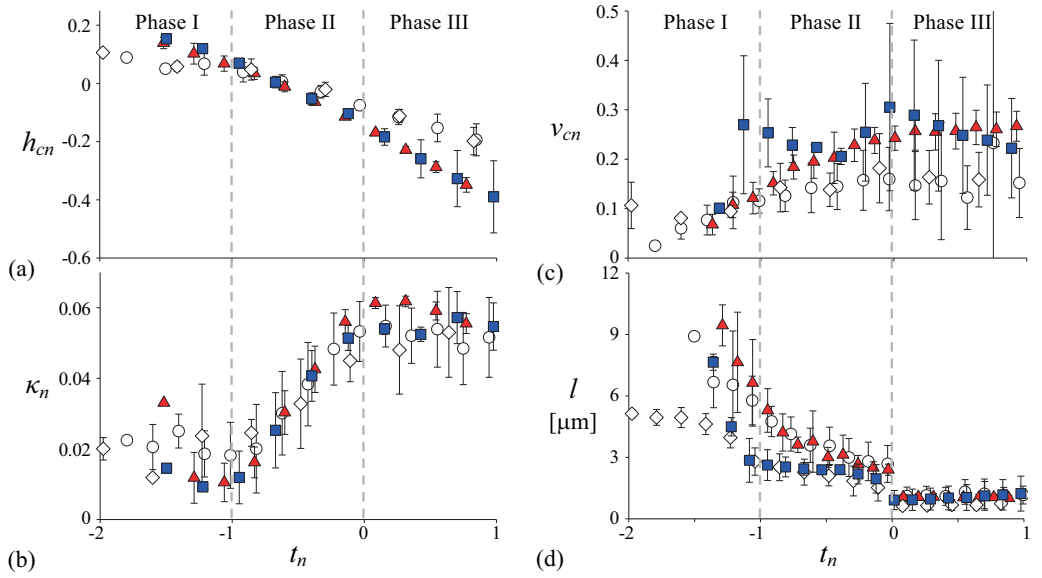

FIG. 9. Diffusion characteristics of a hole geometry at Re = 1850 and 5000: (a) normalized interface center height (h_{cn}); (b) normalized curvature (κ_n); (c) normalized sagging speed (v_{cn}); and (d) diffusion length l for phases I-II (Eq. S4) and III (Eq. S5). ○, $D = 120$ μm (Re = 1850); ▲, 200 μm (Re = 1850); ◇, 120 μm (Re = 5000); ■, 200 μm (Re = 5000).

In addition to the grate geometry, we have measured the diffusion characteristics (interface center height, interface curvature, sagging speed, and diffusion length) of the plastron trapped in the hole geometry as shown in Fig. 9. Here, we varied the hole diameter as $D = 120$ and 200 μm at the Reynolds numbers of Re = 1850 and 5000. Similar to the grate geometry, the interface height decreases with time across phases I–III, while its rate is steeper as the hole diameter increases [Fig. 9(a)]. With the hole geometry, the overall change of interface curvature shows a similar trend to that for the grates but it has relatively less variation across the phases [Fig. 9(b)], indicating that the air-water interface formed on a hole has a higher initial contact angle and a lower advancing contact angle (θ_c). As the hole size increases, the sagging speed becomes faster for both Reynolds numbers, but it tends to saturate earlier for the case of Re = 5000 [Fig. 9(c)]. This seems to be due to the increased wall shear and turbulence in the flow as the Reynolds number of flow over the hydrophobic surface increases. This is also found in the variation of diffusion length, as shown in Fig. 9(d). While the decrease in diffusion length is considerably faster in phase I and becomes mild in phase II, the diffusion length of the same hole diameter is reduced as Re increases. Also, smaller diffusion length is estimated for a smaller hole diameter. Interestingly, the decreasing slope of diffusion length of the hole geometry is larger than that of the grate, which is attributed to the more confined (isolated) geometry of the hole. In less confined geometry such as that of a long grate, the air flow is induced due to the water flow [13], which is thought to contribute to the faster diffusion of air. However, the air flow will not be developed fully in a confined geometry, and thus the diffusion length decreases relatively slowly.

B. Scaling relation of diffusion length

In the previous section, we have shown that the diffusion characteristics of air pockets vary depending on the type and size of the roughness feature, the Reynolds number of the flow over the surface, and the time-dependent phases. While it is highly required to have a practical guideline on the design of roughness feature considering the lifetime of the trapped air on the superhydrophobic surface, here we suggest one approach. Based on the results in Sec. IV A, it is clear that the

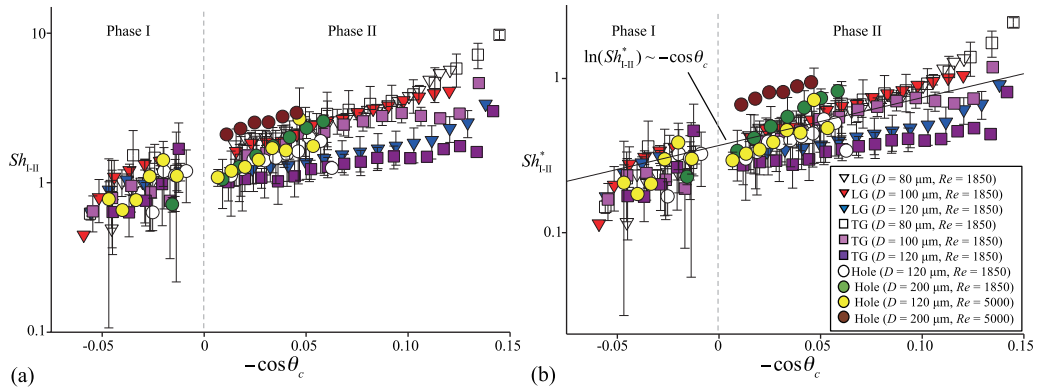

FIG. 10. Interface curvature-dependent variation of nondimensional diffusion length (Sherwood number, $\mathrm{Sh}_{\mathrm{I-II}}$) for phases I and II: (a) $\mathrm{Sh}_{\mathrm{I-II}} = l_\circ/l_{\mathrm{I-II}}$; (b) $\mathrm{Sh}^*_{\mathrm{I-II}} = \mathrm{Sh}_{\mathrm{I-II}}(D/2d)^{1/3}$. In (b), the solid line is $\mathrm{Sh}^*_{\mathrm{I-II}} = 0.4\exp(-7.2\cos\theta_c)$.

diffusion speed is closely related to the interface shape, and thus we discuss phases I-II and III separately. First, we think that the contact angle (θ_c) between the interface and the sidewall of the roughness represents the temporal variation of the interface shape in phases I and II, and we analyzed the dependency of the nondimensional diffusion length (Sherwood number, Sh) on $-\cos\theta_c$ (i.e., dimensionless curvature) (Fig. 10). We chose $-\cos\theta_c$ because it increases as the sagging of the interface progresses, and $-\cos\theta_c = 0$ when the transition from phase I to II occurs. The Sherwood number is defined as the ratio of the convective transfer rate to the diffusion rate as $\mathrm{Sh} = k/k_\circ$. For the present study, k is the convective mass transfer rate of trapped gas (with the water flow) and $k_\circ$ is for the static case (without water flow and only the natural diffusion works). On the other hand, the thin-film theory assumes that when the plastron is exposed to water saturated with air, the diffusion occurs slowly and the diffusion-induced convection perpendicular to the interface can be neglected. As a result, the mass transfer rate is modeled as $k = D_G/l$ [52]. Then the Sherwood number is rewritten as $\mathrm{Sh} = k/k_\circ = (D_G/l)/(D_G/l_\circ) = l_\circ/l$, which is the inverse of the dimensionless diffusion length. Therefore, as the Sherwood number increases, the effect of water flow on the transfer of trapped air increases, compared to the natural diffusion. In phases I and II, we have shown that a single relation [Eq. (11)] can be used to estimate the diffusion length, and thus the Sherwood number is calculated as $\mathrm{Sh}_{\mathrm{I-II}} = l_\circ/l_{\mathrm{I-II}}$. In the present study, we measured the diffusion length ($l_\circ$) in a static condition using the same experimental setup and methods (the only difference is that the water in the channel is stagnant) and the results are shown in Table I (please see the Supplemental Material [51] for the details). As shown in Table I, measured $l_\circ$ is quite a bit smaller than those reported previously [28,29]. Because the diffusion length is affected by various experimental conditions such as the hydrostatic pressure and roughness geometry, it is thus necessary to maintain the consistency of measurement conditions for fair comparison.

As shown in Fig. 10(a), $\mathrm{Sh}_{\mathrm{I-II}}$ tends to increase gradually with $-\cos\theta_c$ for all the cases considered in the present study. While they are similar to each other in phase I, the results from different tested conditions are increasingly scattered as the sagging progresses in phases II. For the grate geometry, in general, the longitudinal grate shows a larger $\mathrm{Sh}_{\mathrm{I-II}}$, but the maximum $\mathrm{Sh}_{\mathrm{I-II}}$ is measured for a transverse grate of $D = 80$ μm, which is the case of maximum curvature. It is also seen that the range of $-\cos\theta_c$ for the hole case is narrower than that of a grate, which indicates that the contact angle variation is smaller for the hole. The difference in the range of $-\cos\theta_c$ corresponds to about a 1.5° difference in θ_c. While this can be considered to be small, it is interesting to see that the critical θ_c for the interface depinning is consistently smaller for the hole geometry. Although this requires more investigation, we suspect that the effects of three-dimensional geometry and/or flow condition may cause the critical θ_c of the interface breakdown to deviate from the nominal advancing contact

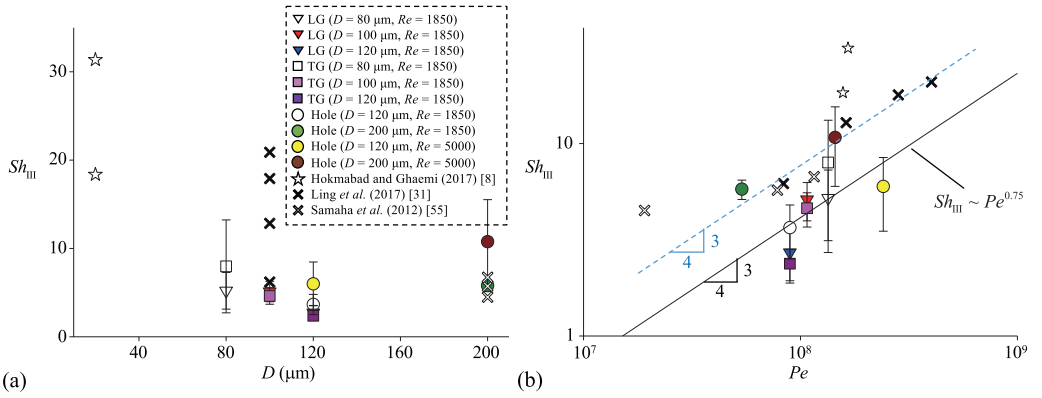

FIG. 11. Variation of nondimensional diffusion length (Sherwood number, $\mathrm{Sh}_{\mathrm{III}} = l_\circ/l_{\mathrm{III}}$) for phase III: (a) in terms of roughness size (D); (b) in terms of Peclet number, $\mathrm{Pe} = (U/D)[(2d)^2/D_g]$. In (b), the solid line is $\mathrm{Sh}_{\mathrm{III}} = 4 \times 10^{-6}\mathrm{Pe}^{3/4}$.

angle of the surface. With the Reynolds number fixed, $\mathrm{Sh}_{\mathrm{I-II}}$ becomes smaller as the roughness size increases and it becomes larger as the Reynolds number increases with a fixed roughness size. Thus, it is consistently found that the diffusion rate is proportional to the Reynolds number but inversely proportional to the structure size, as we have explained in the previous section. As the roughness size appears to be an important parameter to determine the diffusion characteristics, we have modified the Sherwood number as $\mathrm{Sh}^*_{\mathrm{I-II}} = \mathrm{Sh}_{\mathrm{I-II}}(D/2d)^{1/3}$ and plotted its distribution in Fig. 10(b). Here, D is the roughness size and d is the half channel height. As shown in the figure, now the difference between structure sizes is more or less reduced and we suggest that the scaling relation of $\ln(\mathrm{Sh}^*_{\mathrm{I-II}}) \sim -\cos\theta_c$ explains the diffusion characteristics of trapped air pockets in phases I-II. In Fig. 10(b), the solid line shows the relation of $\mathrm{Sh}^*_{\mathrm{I-II}} = 0.4\exp(-7.2\cos\theta_c)$, and the constants were determined by the least-squares error method. The deviation between the proposed model and the measured Sherwood number is largest for the transverse grate of $D = 120\ \mu$m in phase II where $-\cos\theta_c$ is relatively large. In summary, for phases I and II we suggest that the $\mathrm{Sh}_{\mathrm{I-II}}$ strongly depends on the structure size and interface shape (i.e., curvature).

Next, we examine the change of the Sherwood number in phase III, $\mathrm{Sh}_{\mathrm{III}} = l_\circ/l_{\mathrm{III}}$. As a representative value of l_{III}, we use a time-averaged value (compared to phases I and II, the diffusion length shows a smaller variation in phase III). Since the curvature shape is almost constant after the pinchoff in phase III, the roughness size (D) is thought to be an important parameter, and thus the variation of $\mathrm{Sh}_{\mathrm{III}}$ with D is shown in Fig. 11. As shown in Fig. 11(a), for the grate the $\mathrm{Sh}_{\mathrm{III}}$ is inversely proportional to D, but the difference according to the orientation (longitudinal or transverse) is not clear. For the hole cases, there is a small effect of D but $\mathrm{Sh}_{\mathrm{III}}$ changes much with increasing Reynolds number. Previously, the mass diffusion characteristics of a flowing system have been explained by the relationship between the Sherwood number and the Peclet number (Pe) [52,55]. The Peclet number is defined as the ratio of the characteristic shear rate and the diffusion rate. As we have explained above, for phase III, we use the structure size as a characteristic length scale and thus the shear rate can be expressed as U/D, where U is the bulk velocity in the channel flow. The diffusion rate is defined as the ratio of the diffusion coefficient to the square of the characteristic length scale of the mass diffusion, which is known to be related to the channel height [52]. Thus, we define the Peclet number as $\mathrm{Pe} = (U/D)(2d)^2/D_G$. In Fig. 11(b), the change of $\mathrm{Sh}_{\mathrm{III}}$ according to Pe is plotted together with the available data in the literature [31,56]. From their data, we used the appropriate values to calculate the Peclet and Sherwood numbers that we have defined above. Collecting all the data, it is clear that $\mathrm{Sh}_{\mathrm{III}}$ is related to Pe as $\mathrm{Sh}_{\mathrm{III}} \sim \mathrm{Pe}^{3/4}$. As we have explained earlier, we intentionally used a larger size of roughness feature to study the diffusion characteristics. As a result, the data shown in Fig. 11(b) cover a range of Pe (and $\mathrm{Sh}_{\mathrm{III}}$ as well), and

the present scaling relation is valid (the slopes of the dashed and solid lines in the figure are same). It is also noted that some parameters such as the roughness size and reference diffusion length, which were not given explicitly, are estimated from the relevant references. For example, to calculate Sh_{III} for Ling *et al.* [31], we used the value of $l_\circ = 120$ μm from Xu *et al.* [29], who measured diffusion length at a static condition for grate ($D = 50$–150 μm) geometry under a hydrostatic pressure of 1.05–1.2 atm, which is a very similar condition to that of Ling *et al.* [31]. Furthermore, previous studies tried to develop the model for Sh with information on the inner scale of boundary-layer flow; however, the present scaling relation only requires information on the flow and roughness geometry in a physical scale.

To summarize, we have suggested the dependency of diffusion characteristics of plastron on the interface curvature and roughness geometry in phases I and II, in consideration of the temporally varying nature of interface curvature. In phase III, after the depinning of the interface, the interface curvature is maintained almost constant, so the dependency on the flow condition becomes more important to estimate the diffusion characteristics.

V. CONCLUDING REMARKS

In the present study, the wetting process of plastron formed on a fully immersed hydrophobic surface, with various roughness geometries (grates and holes), in the channel flow at $Re = 1850$ and 5000 was directly measured using reflection interference contrast microscopy. Based on the temporally varying three-dimensional air-water interface shape, we proposed that the wetting process of the plastron occurs in three phases, and the diffusion characteristics of the plastron change depending on them. Also, we theoretically formulated the diffusion length for each phase, which can be calculated with the measured interface shape. As a result, we measured that the interface height decreases gradually across the whole phases, while the curvature and diffusion length change during phases I and II, but they are saturated at phase III. Furthermore, these measured parameters showed a different temporal variation depending on the structure size and Reynolds number. To provide a practical relation to estimate the diffusion rate according to different roughness and flow conditions, we suggested two scaling relations of $\ln[Sh_{I-II}(D/2d)^{1/3}] \sim -\cos\theta_c$ for phases I and II and $Sh_{III} \sim Pe^{3/4}$ for phase III, respectively, which showed a good agreement with the present and previous experimental data.

Many previous studies on the flow over the SHPho surfaces have assumed that the air-water interface is initially and/or permanently flat, whereas the present results showed that the air-water interface may form an initially convex shape. The initial condition of the air-water interface formed on the underwater SHPho surface is important not only for predicting the overall wetting process (i.e., lifetime) but also because it directly affects the flow control performance (e.g., drag reduction) [20–25]. Therefore, further studies on the initial shape of the air-water interface depending on the flow condition are needed. Moreover, in order to determine a more precise relation between Sh and Pe or other predetermined parameters, precise velocity measurements of gas and liquid phases as well as the air concentration profile near the plastron are required.

ACKNOWLEDGMENTS

This work was supported by research grants (2016R1C1B2012775 and 2017R1A4A1015523) through the National Research Foundation of Korea (NRF), funded by the Korea government (MSIT) via SNU-IAMD, and also the Institute of Engineering Research and Entrepreneurship at Seoul National University. The authors thank J. S. Khim for access to the DO meter.

[1] C. H. Choi and C.-J. Kim, Large Slip of Aqueous Liquid Flow Over a Nanoengineered Superhydrophobic Surface, Phys. Rev. Lett. **96**, 066001 (2006).

[2] J. P. Rothstein, Slip on superhydrophobic surfaces, Annu. Rev. Fluid Mech. **42**, 89 (2010).

[3] E. Lauga and H. A. Stone, Effective slip in pressure-driven stokes flow, J. Fluid Mech. **489**, 55 (2003).
[4] C. Ybert, C. Barentin, C. Cottin-Bizonne, P. Joseph, and L. Bocquet, Achieving large slip with superhydrophobic surfaces: Scaling laws for generic geometries, Phys. Fluids **19**, 123601 (2007).
[5] C. Lee, C.-H. Choi, and C.-J. Kim, Structured Surfaces for a Giant Liquid Slip, Phys. Rev. Lett. **101**, 064501 (2008).
[6] H. Park, H. Park, and J. Kim, A numerical study of the effects of superhydrophobic surface on skin-friction drag in turbulent channel flow, Phys. Fluids **25**, 110815 (2013).
[7] J. Seo and A. Mani, On the scaling of the slip velocity in turbulent flows over superhydrophobic surfaces, Phys. Fluids **28**, 025110 (2016).
[8] B. V. Hokmabad and S. Ghaemi, Effect of flow and particle-plastron collision on the longevity of superhydrophobicity, Sci. Rep. **7**, 41448 (2017).
[9] R. J. Daniello, N. E. Waterhouse, and J. P. Rothstein, Drag reduction in turbulent flows over superhydrophobic surfaces, Phys. Fluids **21**, 085103 (2009).
[10] B. Woolford, J. Prince, D. Maynes, and B. W. Webb, Particle image velocimetry characterization of turbulent channel flow with rib patterned superhydrophobic walls, Phys. Fluids **21**, 085106 (2009).
[11] E. Aljallis, M. A. Sarshar, R. Datla, V. Sikka, A. Jones, and C.-H. Choi, Experimental study of skin friction drag reduction on superhydrophobic flat plates in high Reynolds number boundary layer flow, Phys. Fluids **25**, 025103 (2013).
[12] H. Park, G. Sun, and C.-J. Kim, Superhydrophobic turbulent drag reduction as a function of surface grating parameters, J. Fluid Mech. **747**, 722 (2014).
[13] Y. Li, K. Alame, and K. Mahesh, Feature-resolved computational and analytical study of laminar drag reduction by superhydrophobic surfaces, Phys. Rev. Fluids **2**, 054002 (2017).
[14] D. Legendre, E. Lauga, and J. Magnaudet, Influence of slip on the dynamics of two-dimensional wakes, J. Fluid Mech. **633**, 437 (2009).
[15] N. Kim, H. Kim, and H. Park, An experimental study on the effects of rough hydrophobic surfaces on the flow around a circular cylinder, Phys. Fluids **27**, 085113 (2015).
[16] J. Lee, H. Kim, and H. Park, Effects of superhydrophobic surfaces on the flow around a NACA0012 hydrofoil at low Reynolds numbers, Exp. Fluids **59**, 111 (2018).
[17] H. Choi, J. Lee, and H. Park, Wake structures behind a rotor with superhydrophobic-coated blades at low Reynolds number, Phys. Fluids **31**, 015102 (2019).
[18] A. I. Ageev, I. V. Golubkina, and A. N. Osiptsov, Application of boundary element method to stokes flows over a striped superhydrophobic surface with trapped gas bubbles, Phys. Fluids **30**, 012102 (2018).
[19] D. Reholon and S. Ghaemi, Plastron morphology and drag of a superhydrophobic surface in turbulent regime, Phys. Rev. Fluids **3**, 104003 (2018).
[20] A. Steinberger, C. Cottin-Bizonne, P. Kleimann, and E. Charlaix, High friction on a bubble mattress, Nat. Mater. **6**, 665 (2007).
[21] J. Hyväluoma and J. Harting, Slip Flow Over Structured Surfaces with Entrapped Microbubbles, Phys. Rev. Lett. **100**, 246001 (2008).
[22] C. J. Teo and B. C. Khoo, Flow past superhydrophobic surfaces containing longitudinal grooves: Effects of interface curvature, Microfluid. Nanofluid. **9**, 499 (2010).
[23] A. M. Davis and E. Lauga, Geometric transition in friction for flow over a bubble mattress, Phys. Fluids **21**, 011701 (2009).
[24] D. G. Crowdy, Analytical formulas for longitudinal slip lengths over unidirectional superhydrophobic surfaces with curved menisci, J. Fluid Mech. **791**, R7 (2016).
[25] D. Crowdy, Slip length for transverse shear flow over a periodic array of weakly curved menisci, Phys. Fluids **29**, 091702 (2017).
[26] B. Emami, A. A. Hemeda, M. M. Amrei, A. Luzar, M. Gad-el-Hak, and H. V. Tafreshi, Predicting longevity of submerged superhydrophobic surfaces with parallel grooves, Phys. Fluids **25**, 062108 (2013).
[27] A. A. Hemeda and H. V. Tafreshi, General formulations for predicting longevity of submerged superhydrophobic surfaces composed of pores or posts, Langmuir **30**, 10317 (2014).
[28] P. Lv, Y. Xue, Y. Shi, H. Lin, and H. Duan, Metastable States and Wetting Transition of Submerged Superhydrophobic Structures, Phys. Rev. Lett. **112**, 196101 (2014).

[29] M. Xu, G. Sun, and C.-J. Kim, Infinite Lifetime of Underwater Superhydrophobic States, Phys. Rev. Lett. **113**, 136103 (2014).
[30] L. Piao and H. Park, Two-dimensional analysis of airwater interface on superhydrophobic grooves under fluctuating water pressure, Langmuir **31**, 8022 (2015).
[31] H. Ling, J. Katz, M. Fu, and M. Hultmark, Effect of Reynolds number and saturation level on gas diffusion in and out of a superhydrophobic surface, Phys. Rev. Fluids **2**, 124005 (2017).
[32] M. S. Bobji, S. V. Kumar, A. Asthana, and R. N. Govardhan, Underwater sustainability of the "cassie" state of wetting, Langmuir **25**, 12120 (2009).
[33] R. Poetes, K. Holtzmann, K. Franze, and U. Steiner, Metastable Underwater Superhydrophobicity, Phys. Rev. Lett. **105**, 166104 (2010).
[34] E. Søgaard, N. K. Andersen, K. Smistrup, S. T. Larsen, L. Sun, and R. Taboryski, Study of transitions between wetting states on microcavity arrays by optical transmission microscopy, Langmuir **30**, 12960 (2014).
[35] Y. Xiang, Y. Xue, P. Lv, D. Li, and H. Duan, Influence of fluid flow on the stability and wetting transition of submerged superhydrophobic surfaces, Soft Matter **12**, 4241 (2016).
[36] E. Karatay, A. S. Haase, C. W. Visser, C. Sun, D. Lohse, P. A. Tsai, and R. G. Lammertink, Control of slippage with tunable bubble mattresses, Proc. Natl. Acad. Sci. (USA) **110**, 8422 (2013).
[37] D. Song, B. Song, H. Hu, X. Du, P. Du, C.-H. Choi, and J. P. Rothstein, Effect of a surface tension gradient on the slip flow along a superhydrophobic air-water interface, Phys. Rev. Fluids **3**, 033303 (2018).
[38] G. Wiegand, K. R. Neumaier, and E. Sackmann, Microinterferometry: three-dimensional reconstruction of surface microtopography for thin-film and wetting studies by reflection interference contrast microscopy (RICM), Appl. Opt. **37**, 6892 (2007).
[39] S. Moulinet and D. Bartolo, Life and death of a fakir droplet: Impalement transitions on superhydrophobic surfaces, Eur. Phys. J. E **24**, 251 (2007).
[40] L. Limozin and K. Sengupta, Quantitative reflection interference contrast microscopy (RICM) in soft matter and cell adhesion, Chem. Phys. Chem. **10**, 2752 (2009).
[41] J. de Ruiter, F. Mugele, and D. van den Ende, Air cushioning in droplet impact. i. dynamics of thin films studied by dual wavelength reflection interference microscopy, Phys. Fluids **27**, 012104 (2015).
[42] J. Laufer, Investigation of turbulent flow in a two-dimensional channel, Tech. Rep. 1053 (NACA Report, 1951).
[43] M. A. Niederschulte, R. J. Adrian, and T. J. Hanratty, Measurements of turbulent flow in a channel at low Reynolds numbers, Exp. Fluids **9**, 222 (1990).
[44] A. F. Stalder, G. Kulik, D. Sage, L. Barbieri, and P. Hoffmann, A snakebased approach to accurate determination of both contact points and contact angles, Colloids Surf., A **286**, 92 (2006).
[45] B. Cortese, S. D'Amone, M. Manca, I. Viola, R. Cingolani, and G. Glgli, Superhydrophobicity due to the hierarchical scale roughness of pdms surface, Langmuir **24**, 2712 (2008).
[46] J. S. Ploem, *Reflection-Contrast Microscopy as a Tool for Investigation of the Attachment of Living Cells to a Glass Surface* (Blackwell, Oxford, 1975).
[47] Q. Kemao, *Windowed Fringe Pattern Analysis* (SPIE, Bellingham, 2013).
[48] X. Zhou, A. G. Podoleanu, Z. Yang, T. Yang, and H. Zhao, Morphological operation-based bi-dimensional empirical mode decomposition for automatic background removal of fringe patterns, Opt. Express **20**, 24247 (2012).
[49] K. G. Larkin, Natural demodulation of two-dimensional fringe patterns. ii. stationary phase analysis of the spiral phase quadrature transform, J. Opt. Soc. Am. A **18**, 1871 (2001).
[50] K. G. Larkin, D. J. Bone, and M. A. Oldfield, Natural demodulation of two-dimensional fringe patterns. i. general background of the spiral phase quadrature transform, J. Opt. Soc. Am. A **18**, 1862 (2001).
[51] See Supplemental Material at http://link.aps.org/supplemental/10.1103/PhysRevFluids.4.074001 for additional information on experimental methods and the derivation of diffusion length models.
[52] E. L. Cussler, *Diffusion: Mass Transfer in Fluid Systems* (Cambridge University Press, Cambridge, 2009).
[53] R. F. Probstein, *Physicochemical Hydrodynamics: An Introduction* (Butterworths, Stoneham, 1989).

[54] R. Costantini, J.-P. Mollicone, and F. Battista, Drag reduction induced by superhydrophobic surfaces in turbulent pipe flow, Phys. Fluids **30**, 025102 (2018).

[55] A. S. Haase and R. G. Lammertink, Heat and mass transfer over slippery, superhydrophobic surfaces, Phys. Fluids **28**, 042002 (2016).

[56] M. A. Samaha, H. V. Tafreshi, and M. Gad-el-Hak, Influence of flow on longevity of superhydrophobic coatings, Langmuir **28**, 9759 (2012).